ADVANCED FUNCTIONAL MATERIALS
www.afm-journal.de

Modulating Interfacial Potential Gradients in Metal–Carbon Catalysts via Phase-Engineering for Lithium–Sulfur Batteries

Ji-Oh Kim, Hengquan Guo, Seonghee Kim, Jae Bin Park, Seongwook Chae, Taekyun Kwon, Seungjo Hong, Byeong Jin Kim, Guadalupe Arturo De la Garza Gonzalez, Minjoon Park, Jae Ho Kim, Oi Lun Li, Seung Geol Lee,* and Jin Hong Lee**

Lithium–sulfur batteries (LSBs) suffer from sluggish sulfur redox kinetics and severe shuttling of lithium polysulfides (LiPSs). Although increasing the active surface area of metal–carbon electrocatalysts improves LiPSs redox kinetics, unlocking further improvements requires enhancing intrinsic catalytic activity of the expanded active sites. Herein, a fundamental investigation is conducted to enhance the catalytic capability of active sites by controlling the crystalline phase of the encapsulated cobalt. Theoretical calculations reveal that modulating the cobalt crystalline phase from HCP to FCC enhances the interfacial potential gradient, which serves as the driving force for electron transfer from cobalt to carbon shell at the metal–carbon interface. Guided by this insight, a deliberate temperature-controlled annealing is conducted to regulate the thermodynamically stable phase of cobalt, while alleviating the structural variations of carbon shells. Comprehensive spectroscopic analyses confirm that this approach modulates the electron band structure of the carbon shell, elevating the valence band maximum and enriching the electronic density near the Fermi level. As a result, F-Co@NC exhibits superior LiPSs redox kinetics and strong LiPSs adsorption capability, which in turn improves the electrochemical performance of LSBs. This work presents a broadly applicable design strategy for advancing metal–carbon electrocatalysts, capable of delivering synergistic effects with previous studies.

1. Introduction

High-energy-density energy storage systems have become indispensable for the advancement of modern and emerging applications, including electric vehicles, drones, and humanoid robots, which demand compact, lightweight, and long-lasting power sources for efficient and autonomous operation.[1–3] As these technologies continue to evolve and proliferate, the pursuit of next-generation rechargeable batteries with enhanced energy density, prolonged cycling stability, and improved safety has attracted unprecedented attention. Lithium–sulfur batteries (LSBs), utilizing sulfur as the cathode active material, have emerged as one of the most promising next-generation energy storage systems, due to their exceptionally high theoretical specific capacity (1675 mAh g^{-1}) and ultrahigh energy density (≈2600 Wh kg^{-1}) originating from the multielectron redox reaction (S_8 + 16 Li^+ + 16 e^- ↔ 8 Li_2S), as well as the natural abundance and low cost of sulfur.[4–5] However, the practical implementation of LSBs remains hindered by several challenges. The intrinsically insulating nature of both elemental sulfur (S_8) and its discharge products (Li_2S_2, Li_2S), combined with the sluggish redox kinetics of lithium polysulfides (LiPSs), significantly limits charge transport and redox reaction reversibility.[6–8] Moreover, the spontaneous diffusion of soluble LiPSs toward the lithium metal anode induces a severe shuttle effect, leading to continuous loss of active materials, low

J.-O. Kim, J. B. Park, T. Kwon, S. Hong, B. J. Kim, J. H. Lee
School of Chemical Engineering
Pusan National University
Busan 46241, Republic of Korea
E-mail: jinhong.lee@pusan.ac.kr

The ORCID identification number(s) for the author(s) of this article can be found under https://doi.org/10.1002/adfm.202525392

DOI: 10.1002/adfm.202525392

H. Guo, S. Chae, S. G. Lee
Department of Materials Science and Engineering
Ulsan National Institute of Science and Technology (UNIST)
Ulsan 44919, Republic of Korea
E-mail: seunggeol.lee@unist.ac.kr

S. Kim, G. A. De la Garza Gonzalez, O. L. Li
School of Materials Science and Engineering
Pusan National University
Busan 46241, Republic of Korea
E-mail: helenali@pusan.ac.kr

M. Park, J. H. Kim
School of Transdisciplinary Engineering
Department of Nano Fusion Technology
Research Center of Energy Convergence Technology
Pusan National University
Busan 46241, Republic of Korea

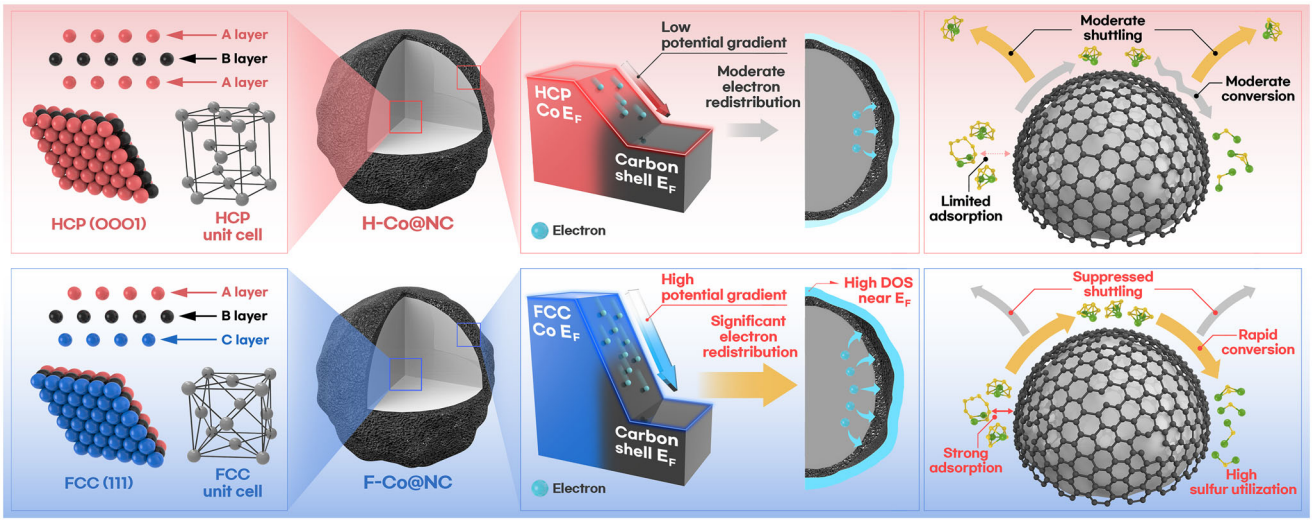

Figure 1. Schematic illustration of the phase-engineered cobalt–carbon composites (F-Co@NC and H-Co@NC) showing the modulation of interfacial potential gradients and their influence on adsorption, shuttling, and conversion behavior of LiPSs.

coulombic efficiency, and considerable lithium corrosion, ultimately resulting in poor sulfur utilization and rapid capacity fading of LSBs.[9–13] As such, tackling these obstacles requires not only the promotion of efficient electrochemical conversion of sulfur species but also effective suppression of the LiPSs shuttling behavior.

In response to these issues, extensive efforts have been devoted to the development of electrocatalysts using transition metals such as Co, Ni, and Fe, since they exhibit superior electron transfer capability and chemical affinity toward LiPSs, thereby enabling the acceleration of redox conversion kinetics of LiPSs as well as mitigating LiPSs shuttling behavior.[14–22] Nevertheless, transition metal catalysts are often constrained by the limited exposure of active sites arising from the aggregation of metal particles and their surface passivation, which reduces the catalytically active surface area and deteriorates their catalytic efficiency during prolonged cycling in LSBs.[23–27] To address these limitations, considerable research has focused on the design of carbon–transition metal composite nanomaterials. These hybrid structures not only improve the dispersion of metal active sites within a conductive carbon matrix but also protect them from surface passivation through physical encapsulation.[28–33] This structural integration enables sustained exposure of active sites and preserves catalytic integrity over extended cycling. Consequently, carbon–metal composites have demonstrated superior long-term electrocatalytic activity toward LiPSs redox reactions, contributing to enhanced reaction kinetics and cycling stability in LSBs.

To further improve the catalytic performance of carbon–metal composites in LSBs, various strategies have been explored, including control over the particle size of the metal species, regulation of their spatial distribution, and even incorporation of multiple metal components.[34–39] However, little attention has been paid to controlling the crystalline phase of the embedded metal, even though variations in atomic arrangement and lattice symmetry can alter the metal-to-carbon electron transfer behavior, thereby modulating interfacial charge redistribution and ultimately tailoring the electronic structure and electrocatalytic properties of the carbon shells.

Herein, we report a fundamental investigation of interfacial electronic structure modulation enabled by crystalline phase control of metal nanoparticles encapsulated within a carbon shell. A carbon–metal composite electrocatalyst was synthesized with cobalt as the metal component, a widely employed transition metal via plasma engineering. Our previous studies have successfully applied plasma engineering to fabricate homogeneous anchoring of transition metal nanoparticles within the carbon matrix, ensuring uniform dispersion and improved interfacial contact during subsequent annealing.[40,41] In the current study, we have applied a similar synthesis route for a cobalt core–carbon shell as the composite electrocatalysts (Experimental Section). As illustrated in **Figure 1**, temperature-controlled annealing modulates the dominant crystalline phase of cobalt, yielding a face-centered cubic (FCC)-dominant or hexagonal close-packed (HCP)-dominant cobalt–carbon composites (denoted as F-Co@NC and H-Co@NC, respectively). Theoretical calculations and experimental analyses reveal that FCC cobalt exhibits a higher Fermi level (E_F) than HCP cobalt, leading to a narrower energy gap between the valence band maximum (VBM) of the encapsulating carbon shell and its E_F. Such an upward shift of the VBM toward the E_F increases the density of electronic states near E_F, thereby enhancing the electron-donating capability of the carbon shell. This cobalt phase-induced modulation of the carbon shell's electronic structure facilitates charge transport and strengthens chemical affinity toward LiPSs. Consequently, F-Co@NC accelerates the sluggish redox kinetics of sulfur species and effectively mitigates the LiPSs shuttle effect. These findings highlight that crystalline phase engineering of encapsulated metal centers serves as an effective strategy to regulate interfacial electronic properties and enhance the electrocatalytic performance of carbon–metal composites in LSBs, thereby providing meaningful guidance for the rational design of electrocatalysts for LSBs.

2. Results and Discussion

First, we hypothesized that controlling the crystalline phase of the encapsulated cobalt could modulate its electron transfer behavior to the surrounding carbon shells through phase-induced variations in the E_F. To corroborate this hypothesis, a density functional theory (DFT)-based comparative examination of the electrostatic potential distribution curves of FCC cobalt, HCP cobalt, and carbon shell was performed. As illustrated in Figure S1 (Supporting Information), both FCC and HCP cobalt exhibited higher E_F values compared to the carbon shell, which can lead to the spontaneous electron transfer from cobalt to the carbon shell. Notably, FCC cobalt demonstrated a higher E_F than HCP cobalt, indicating a stronger electron-donating capability of FCC cobalt. Consistently, the total density of states (TDOS) of bare FCC-Co and HCP-Co (Figure S2, Supporting Information) reveals a higher DOS near the E_F and an upshifted 3d-band center for FCC-Co relative to HCP-Co, indicating a greater intrinsic tendency of the FCC phase to donate electrons. To elucidate the phase-dependent electron redistribution behavior, charge density difference diagrams for the carbon shells encapsulating cobalt with different crystalline phases were investigated. A model consisting of three Co layers and one carbon layer was employed to simulate the interfacial behavior, which has been adopted in a previous study.[42] Each of the carbon composites encapsulating FCC cobalt (denoted as F-Co@NC) and HCP cobalt (denoted as H-Co@NC) was constructed as illustrated in Figure S3 (Supporting Information). We confirmed that F-Co@NC exhibited a higher electron density compared to H-Co@NC, indicating a greater extent of electron transfer from FCC cobalt to the carbon shell than from HCP cobalt (Figure S4, Supporting Information).[43] Moreover, according to the Bader charge analysis, ≈2.04 e^- is transferred from Co to the N-doped carbon in F-Co@NC, compared with 1.92 e^- in H-Co@NC.[44] Based on these results, the electrostatic potential distribution curves for F-Co@NC and H-Co@NC were further investigated. As shown in **Figures 2**a and S5 (Supporting Information), the F-Co@NC exhibited a higher E_F value than H-Co@NC, suggesting that F-Co@NC, through greater electron transfer from cobalt to carbon shells, exhibits superior electron-donating capability.

To promote the redox kinetics of LiPSs in LSBs, the number of electrons located near the E_F of the electrocatalyst is crucial, as they can be readily transferred to the LiPSs.[45] As presented in Figure 2b,c, the density of states (DOS) for both F-Co@NC and H-Co@NC spanned across the E_F, confirming their metallic nature. However, when compared with H-Co@NC, the F-Co@NC was characterized by a more metallic nature and an increased DOS at the E_F, which could be attributed to the intensified charge redistribution between cobalt and carbon shell due to the superior electron-donating property of FCC cobalt.

Then, we simulated the anchoring behavior of Li_2S_x (x = 1, 2, 4, 6, 8) on F-Co@NC and H-Co@NC, and their adsorption energies were evaluated. The side and top views of the most stable adsorption configurations are presented in Figure 2d, Figures S6 and S7 (Supporting Information). For both F-Co@NC and H-Co@NC, the optimized structures showed that all LiPSs species were anchored on the carbon surface encapsulating cobalt. The binding energies ranged from −0.41 to −1.21 eV for the soluble Li_2S_x species (x = 4, 6, 8), while for the later-stage insoluble species, specifically Li_2S_2 and Li_2S, the binding energies increase to a range of −0.96 to −1.39 eV, indicating significant chemisorption characteristics of solid LiPSs species. This increase in the binding strength of LiPSs during the reduction process is consistent with previously reported studies.[46,47] Especially, as shown in Figure 2e, we confirmed that the binding strength of all LiPSs with F-Co@NC was higher than with H-Co@NC. This indicates that F-Co@NC interacts more strongly with LiPSs than H-Co@NC, which potentially contributes to mitigating the shuttling behavior of LiPSs during the repeated charge and discharge processes. Subsequently, the projected density of states (PDOS) of F-Co@NC and H-Co@NC with adsorbed LiPSs was further analyzed to gain deeper insight into their adsorption behavior. As shown in Figure S8 (Supporting Information), the p orbitals of carbon in F-Co@NC exhibited greater overlap with the p orbitals of sulfur compared to those in H-Co@NC, indicating stronger orbital hybridization. These results demonstrate that the enhanced electron density in F-Co@NC due to stronger electron redistribution facilitates LiPSs adsorption, which could promote subsequent redox conversion of LiPSs.[48] We also conducted charge-density-difference (CDD) and Bader charge analyses (Figures S9 and S10, Supporting Information).[49] The CDD maps reveal distinct interfacial charge redistribution and polarization upon Li_2S_x adsorption. The Bader analysis further indicates that the F-Co@NC surface gains electrons upon LiPSs adsorption, showing a larger charge transfer in F-Co@NC compared to H-Co@NC for each adsorbed LiPSs species, with values ranging from 1.21 to 1.06 e^- for F-Co@NC and from 1.08 to 1.04 e^- for H-Co@NC.

The superior Li^+ diffusion capability of the electrocatalyst is considered a critical factor in accelerating the redox kinetics of LiPSs.[50] Thus, we implemented the geometrical configurations of the Li^+ diffusion path between the most stable site and a nearby stable site to estimate the diffusion energy barrier of Li^+ on F-Co@NC and H-Co@NC (Figure 2f,g; detailed configurations are presented in Figures S11 and S12, Supporting Information). For F-Co@NC, the energy barrier of Li^+ migration along the diffusion pathway was only 0.21 eV, which was significantly lower than that of H-Co@NC (0.55 eV), indicating the superior Li^+ transport on the F-Co@NC. After verifying the strong LiPSs adsorption capability and the enhanced Li^+ transport on F-Co@NC, the comprehensive Gibbs free energy calculation for sulfur species along the entire reduction process from S_8 to Li_2S was conducted. It is worth noting that, although the conversion from Li_2S_2 to Li_2S contributes significantly to the discharge capacity of LSBs, it also serves as the rate-determining step due to the sluggish growth of Li_2S, which originates from its intrinsically low electronic conductivity.[51,52] As shown in Figure 2h and F-Co@NC exhibited a significantly lower energy barrier (0.73 eV) for the Li_2S_2-to-Li_2S conversion compared to H-Co@NC (1.28 eV), indicating that reduction of LiPSs is thermodynamically more favorable on F-Co@NC. This reduced barrier by F-Co@NC could accelerate Li_2S deposition, promoting the discharge process in LSBs.

The oxidation behavior of Li_2S is as important as its formation during LiPS reduction, given that it plays a key role in alleviating electrocatalyst passivation and regulating the overall redox kinetics in LSBs.[53] Accordingly, we simulated the decomposition process of Li_2S on both F-Co@NC and H-Co@NC and calculated the corresponding energy barrier (Figure 2i,j; detailed

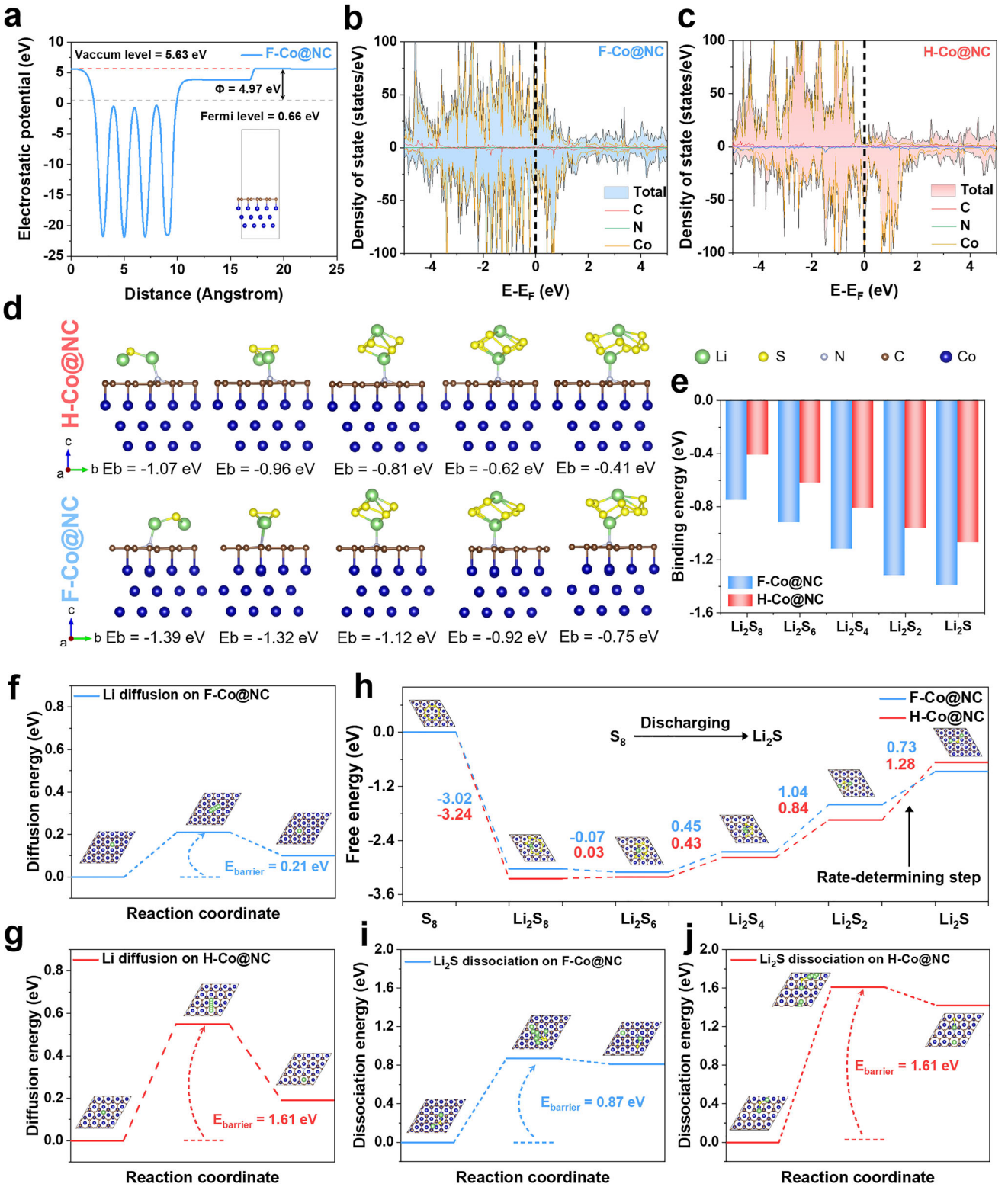

Figure 2. a) Electrostatic potential distribution curve of F-Co@NC. Density of states of b) F-Co@NC and c) H-Co@NC. d) The optimized atomic configurations of adsorbed LiPSs (Li_2S_8, Li_2S_6, Li_2S_4, Li_2S_2, and Li_2S) on F-Co@NC and H-Co@NC surfaces. e) Calculated binding energies between LiPSs and F-Co@NC and H-Co@NC surfaces. Energy barrier profiles for Li^+ diffusion on f) F-Co@NC and g) H-Co@NC. h) Gibbs free energy profiles and corresponding adsorption models for the reduction from S_8 to Li_2S on F-Co@NC and H-Co@NC. Energy barrier profile for Li_2S dissociation on i) F-Co@NC and j) H-Co@NC.

configurations are presented in Figures S13 and S14, Supporting Information). We confirmed that F-Co@NC exhibited a lower dissociation barrier for Li_2S (0.87 eV) compared to the H-Co@NC (1.61 eV), demonstrating its superior oxidation capability toward Li_2S. The above systematic calculations suggest that controlling the crystalline phase of cobalt toward the FCC structure could significantly improve the catalytic activity on redox kinetics of LiPSs.

Motivated by the theoretically predicted catalytic advantages of phase engineering, we proceeded to design cobalt–carbon composites with tunable crystalline phases to experimentally validate the phase-dependent catalytic behavior. Given that cobalt generally exists in an HCP crystal structure under ambient conditions, whereas thermal annealing at sufficiently high temperatures enables its transformation into the FCC structure, we aimed to prepare cobalt–carbon composites with different crystalline phases by precisely regulating the annealing temperature, while minimizing variations in the carbon matrix characteristics such as surface area and D/G ratio to effectively focus on the influence of the cobalt phase on the catalytic properties.[54–57] Since the phase transition of cobalt from HCP to FCC structure involves lattice shear and a change in shape, the transformation of cobalt encapsulated within a rigid carbon shell is hindered by the mechanical constraints imposed by the carbon matrix, leading to a higher transition temperature of ≈700 °C compared to the typical transition temperature for pure cobalt.[58,59] Accordingly, homogeneous cobalt–carbon precursors formed via plasma treatment were annealed at 600 and 700 °C, respectively, and X-ray diffraction (XRD) analysis was first conducted to determine the crystalline phase of cobalt in each composite. As shown in **Figure 3a**, the sample annealed at 600 °C displayed three pronounced diffraction peaks at 41.6°, 44.7°, and 47.5°, corresponding to the HCP Cobalt, indicating that the HCP is the dominant crystalline phase of cobalt in the sample annealed at 600 °C (hereafter denoted as H-Co@NC). In contrast, the sample annealed at 700 °C exhibited a dominant peak at 44.2° and an additional reflection at 51.5° was observed, both assigned to the FCC cobalt, while the peaks at 41.6° and 47.5° were significantly attenuated. These changes demonstrate that regulating the annealing temperature from 600 to 700 °C effectively leads to a transformation of the prevailing cobalt phase in the sample from HCP to FCC (hereafter denoted as F-Co@NC).[60,61] To quantify the fraction of FCC and HCP structures in both F-Co@NC and H-Co@NC, the Rietveld refinement was further conducted. Rietveld refinements of the XRD patterns obtained by Highscore-Plus, and crystallographic details of the structure model used in Rietveld refinements were summarized in Tables S1 and S2 (Supporting Information). As shown in Figure S15 (Supporting Information), the FCC and HCP phase fractions in F-Co@NC were approx≈82.2% for FCC and 17.8% for HCP, respectively, whereas H-Co@NC was determined to be HCP single-phase within the detection limit due to the absence of a detectable characteristic peak of FCC cobalt at 51.5°. This result confirms again that the annealing temperature of 700 °C could effectively transform the dominant crystalline phase of cobalt from HCP to FCC with mild elevation of annealing temperature.

The SEM images of F-Co@NC and H-Co@NC particles showed that both samples demonstrated similar morphology (Figure 3b; Figure S16, Supporting Information). Since the surface area of the carbon matrix could affect the catalytic performance of the electrocatalyst by providing more active sites for LiPSs adsorption and conversion, we evaluated the Brunauer–Emmett–Teller (BET) surface area and porosity of both samples using N_2 adsorption/desorption isotherms.[62] As shown in Figure S17 and Table S3 (Supporting Information), F-Co@NC and H-Co@NC exhibited comparable surface area and pore size distributions. To further evaluate the structural characteristics of the carbon shells in each sample, Raman spectroscopy was performed (Figure 3c). The two distinct peaks located at 1340 and 1582 cm^{-1} correspond to the D and G bands of the carbon shell, respectively.[63] The D/G intensity ratios of F-Co@NC (0.90) and H-Co@NC (0.92) were found to be nearly identical, indicating that the carbon shells were not significantly altered despite the phase transition of the embedded cobalt and the change in annealing temperature. In addition, we conducted Raman mapping analyses for both F-Co@NC and H-Co@NC samples to examine the structural homogeneity of the carbon frameworks. As shown in Figure S18 (Supporting Information), the D/G intensity ratios across the mapped areas were generally comparable with minimal spatial variation, confirming that the carbon shells of both samples exhibit uniform structure.

To gain an in-depth understanding of the nanostructural characteristics of the F-Co@NC and H-Co@NC, transmission electron microscopy (TEM) was carried out. As shown in Figure 3d,e, both F-Co@NC and H-Co@NC featured cobalt nanoparticles with a diameter of ≈20 nm, encapsulated within graphitic carbon shells. Notably, both samples displayed a similar interlayer spacing of graphitic carbon shells (0.37 nm), further confirming the absence of noticeable changes in the graphitic structure of carbon shells induced by the phase transition of cobalt particles (Figure 3f,g). As shown in Figure 3h, the cobalt particle in F-Co@NC exhibited lattice spacings of 0.176 and 0.206 nm, corresponding to the (200) and (111) planes of FCC cobalt, respectively. In contrast, the cobalt particle in H-Co@NC showed a lattice spacing of 0.193 nm, assigned to HCP cobalt.[64,65] These results provide additional evidence for the successful regulation of the dominant crystalline phase of cobalt via appropriate thermal treatment, while minimizing structural alteration of the carbon shell. As presented in Figure 3j and Figure S19 (Supporting Information), EDS elemental mapping from the TEM images of F-Co@NC and H-Co@NC revealed that the cobalt particles and heteroatoms, such as N and O, were uniformly distributed throughout the carbon substrate.

To elucidate the chemical composition of F-Co@NC and H-Co@NC, X-ray photoelectron spectroscopy (XPS) was performed. Survey spectra of F-Co@NC and H-Co@NC confirmed that both samples comprise Co, C, N, and O (Figure S20, Supporting Information). As summarized in Table S4 (Supporting Information), the atomic percentages of N and O in F-Co@NC were lower than those in H-Co@NC, reflecting the higher annealing temperature applied to F-Co@NC. High-resolution N 1s spectra of both materials were deconvoluted into five components at 398.5 eV (pyridinic N), 399.9 eV (pyrrolic N), 400.7 eV (pyridonic N), 401.3 eV (graphitic N), and 403.3 eV (oxidized N) (Figure S21, Supporting Information).[66,67] Compared with H-Co@NC, F-Co@NC exhibited a lower peak intensity corresponding to pyrrolic N, indicating thermally induced conversion of the less-stable pyrrolic sites into pyridinic or graphitic configurations. The C 1s spectra displayed five characteristic peaks at

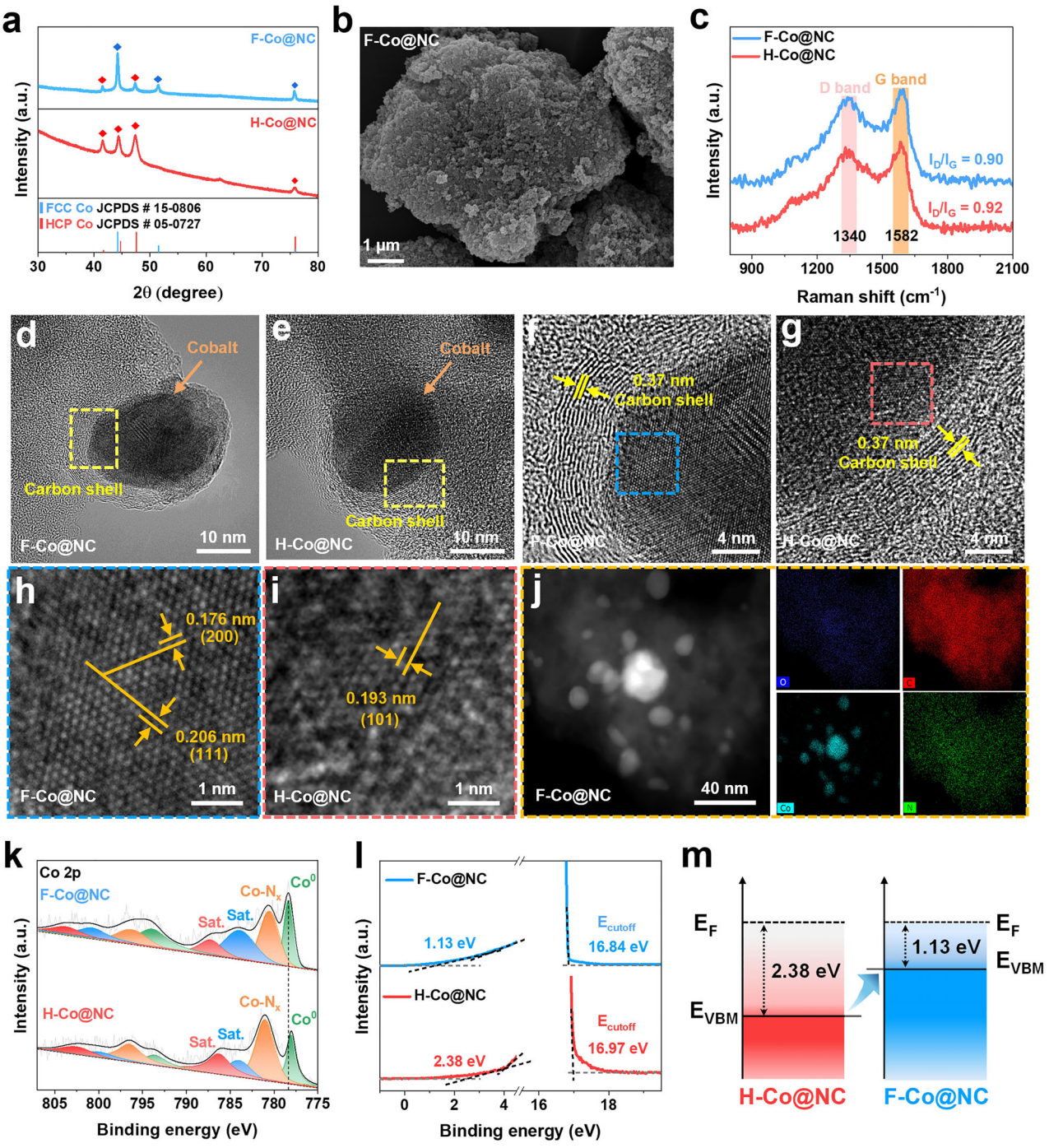

Figure 3. a) XRD patterns of F-Co@NC and H-Co@NC. b) SEM image of F-Co@NC. c) Raman spectra of F-Co@NC and H-Co@NC. TEM images of d) F-Co@NC and e) H-Co@NC. HRTEM images of f,h) F-Co@NC and g,i) H-Co@NC. j) TEM and elemental mapping images of F-Co@NC. k) XPS spectra of Co 2p for F-Co@NC and H-Co@NC. l) UPS spectra of F-Co@NC and H-Co@NC. m) Schematic illustration of band structures of F-Co@NC and H-Co@NC.

284.5, 285.6, 286.7, 288.0, and 289.4 eV, corresponding to C = C/C–C, C = N, C–N, N–C = O, and O = C–O bonds, respectively (Figure S22, Supporting Information).[68] In agreement with the N 1s analysis, the intensity of the C–N peak decreased in F-Co@NC, further corroborating the transformation of pyrrolic N into more thermodynamically stable nitrogen species. Furthermore, we confirmed that the peak intensity of C = N also reduced, indicating the presence of fewer N species in F-Co@NC compared to H-Co@NC. As shown in Figure 3k, the Co 2p of F-Co@NC and H-Co@NC exhibited four peaks, corresponding to Co^0, Co-N_x, and two satellite peaks.[69] The intensity of the Co-N_x peak from F-Co@NC was lower than that from H-Co@NC,

indicating reduced content of N species in F-Co@NC, consistent with the above results. Notably, the Co^0 peak in F-Co@NC (780.3 eV) appeared at a higher binding energy compared to that in H-Co@NC (780.0 eV). This peak shift toward higher binding energy implies that a greater degree of electron transfer occurred from metallic cobalt to the carbon shell.[70]

The local electron redistribution at the interface between cobalt and carbon shells could affect the electronic band structure.[71,72] To thoroughly investigate the changes in the electronic band structure of F-Co@NC and H-Co@NC resulting from the crystalline phase of embedded cobalt particles, we conducted ultraviolet photoelectron spectroscopy (UPS) measurements (Figure 3l). The cutoff energies (E_{cutoff}) of F-Co@NC and H-Co@NC were determined to be 16.84 and 16.97 eV, respectively, and the work functions (Φ) of each sample were calculated using Equation (1):

$$\Phi = h\nu - \left|\left(E_{cutoff}\right) - E_F\right| \quad (1)$$

where h is Planck's constant, ν is the frequency of the incident photon, and E_F is the Fermi energy. We confirmed that the work function of H-Co@NC (4.23 eV) and F-Co@NC (4.36 eV) exhibited only a marginal difference, which could be attributed to the difference in heteroatom contents of N and O atoms in H-Co@NC.[73–75] By contrast, we found that the energy difference between the valence band maximum energy (E_{VBM}) and E_F of F-Co@NC was 1.13 eV, which was significantly smaller than that of H-Co@NC (2.38 eV). As illustrated in Figure 3m, constructed based on the results of UPS, the valence band edge of F-Co@NC was located closer to the E_F compared with that of H-Co@NC. This suggests that greater electron transfer from FCC cobalt to the carbon shell enables facile electron exchange across the band gap, which in turn could enhance both the adsorption and conversion kinetics of LiPSs.[76] These results imply that regulating the crystalline phase of cobalt to the FCC structure could enhance the catalytic activity of electrocatalysts that comprise carbon and cobalt.

To evaluate the impact of the crystalline phase of cobalt encapsulated in the carbon shell on the electrochemical performance of LSBs, F-Co@NC and H-Co@NC were coated onto a commercial polypropylene (PP) separator and incorporated into the LSBs. As presented in Figure S23 (Supporting Information), the F-Co@NC and H-Co@NC coating layers were uniformly integrated onto the PP separator, maintaining good mechanical adhesion without delamination, even after repeated bending deformation. Surface SEM images of the modified separators showed similar morphologies for the F-Co@NC and H-Co@NC coating layers (Figure S24, Supporting Information). EDS elemental mapping of both samples demonstrated the uniform distribution of cobalt elements, confirming the homogeneous distribution of F-Co@NC and H-Co@NC in the coating layers (Figure S25, Supporting Information). Cross-sectional SEM images of the modified separators revealed that the thickness of the F-Co@NC and H-Co@NC layers was ≈10 µm (Figure S26, Supporting Information). Subsequently, the effects of these modified separators with F-Co@NC and H-Co@NC on the electrochemical performance of LSBs were systematically investigated. First, the cells with F-Co@NC and H-Co@NC were applied for cyclic voltammetry (CV) tests in the voltage range of 1.7–2.8 V (vs Li/Li^+) at a scan rate of 0.1 mV s^{-1} (**Figure 4a**). The CV curves of both cells exhibited two cathodic peaks at ≈2.2 V (Peak A) and 1.9 V (Peak B). These peaks are assigned to the stepwise reduction of solid sulfur (S_8) to soluble long-chain LiPSs (Li_2S_x, $4 \le x \le 8$), followed by further reduction to insoluble Li_2S_2 and Li_2S, respectively. Additionally, a broad anodic peak observed ≈2.4 V (Peak C) is attributed to the oxidation of solid Li_2S_2 and Li_2S back to soluble LiPSs, and eventually solid S_8.[77] We confirmed that the cell with F-Co@NC exhibited higher peak currents for all redox transitions and a narrower voltage gap between Peak B and Peak C. In addition, as shown in Figure S27 (Supporting Information), both reduction peaks of the F-Co@NC cell appeared at higher potentials, while the oxidation peak shifted toward a lower potential. These results indicate the enhanced LiPSs conversion of the cell with F-Co@NC compared with that of H-Co@NC. Furthermore, the cell with F-Co@NC also exhibited smaller Tafel slopes across all three redox processes, providing additional evidence for the accelerated redox reaction of sulfur species in the cell with F-Co@NC.

To further elucidate the effect of the intensified charge redistribution-induced enhancement in the electron-donating ability of F-Co@NC on the redox kinetics of LiPSs, the electrochemical performance of the cells under different current densities was evaluated. As shown in Figure 4b, the cell with F-Co@NC delivered the highest specific capacity across all current densities from 0.2 C to 2.0 C, compared to those with H-Co@NC and PP separator. This enhancement became more pronounced as the charge/discharge rate increased, indicating that the superior electron transfer properties of F-Co@NC effectively facilitate the conversion of LiPSs even under high-rate conditions. To gain a deeper understanding of the conversion behavior of LiPSs during the charge/discharge processes, galvanostatic charge–discharge (GCD) profiles at various current densities are presented in Figure 4c and Figure S28 (Supporting Information). The capacity in the high-voltage plateau (designated as Q_1) is ascribed to the reduction of solid S_8 to soluble LiPSs, whereas the capacity in the low-voltage plateau (designated as Q_2) corresponds to the subsequent reduction of soluble LiPSs to solid Li_2S_2 and Li_2S species. Thus, the Q_2/Q_1 ratio provides a meaningful parameter to evaluate the reduction efficiency of LiPSs.[78] As displayed in Figure 4d, the cell with F-Co@NC exhibited the highest Q_2/Q_1 ratio among the cells with H-Co@NC and PP separator at all current densities. This indicates that F-Co@NC promotes the conversion of liquid LiPSs into solid Li_2S_2/Li_2S, thereby enhancing the efficiency of the overall reduction process. Moreover, we confirmed that the overpotential of the cell with F-Co@NC was significantly lower than that of the cells with H-Co@NC and PP separator across all tested current densities, further verifying the accelerated redox kinetics of LiPSs enabled by the superior electrocatalytic capability of F-Co@NC (Figure 4e).

Subsequently, to elucidate the influence of F-Co@NC on the long-term cycling behavior of LSBs, the cycling stability of the cells with F-Co@NC, H-Co@NC, and PP separator was evaluated. As shown in Figure 4f, the cell with F-Co@NC exhibited superior cycling stability compared to those with H-Co@NC and PP. After 100 cycles at 0.2 C, the cell with F-Co@NC retained a specific capacity of 949.5 mAh g^{-1}, with a sulfur utilization of 56.6%. In contrast, the cells with H-Co@NC and PP separator maintained a lower specific capacity of 792.8 and 635.9 mAh g^{-1}, respectively, with lower sulfur utilization of only 47.3% and

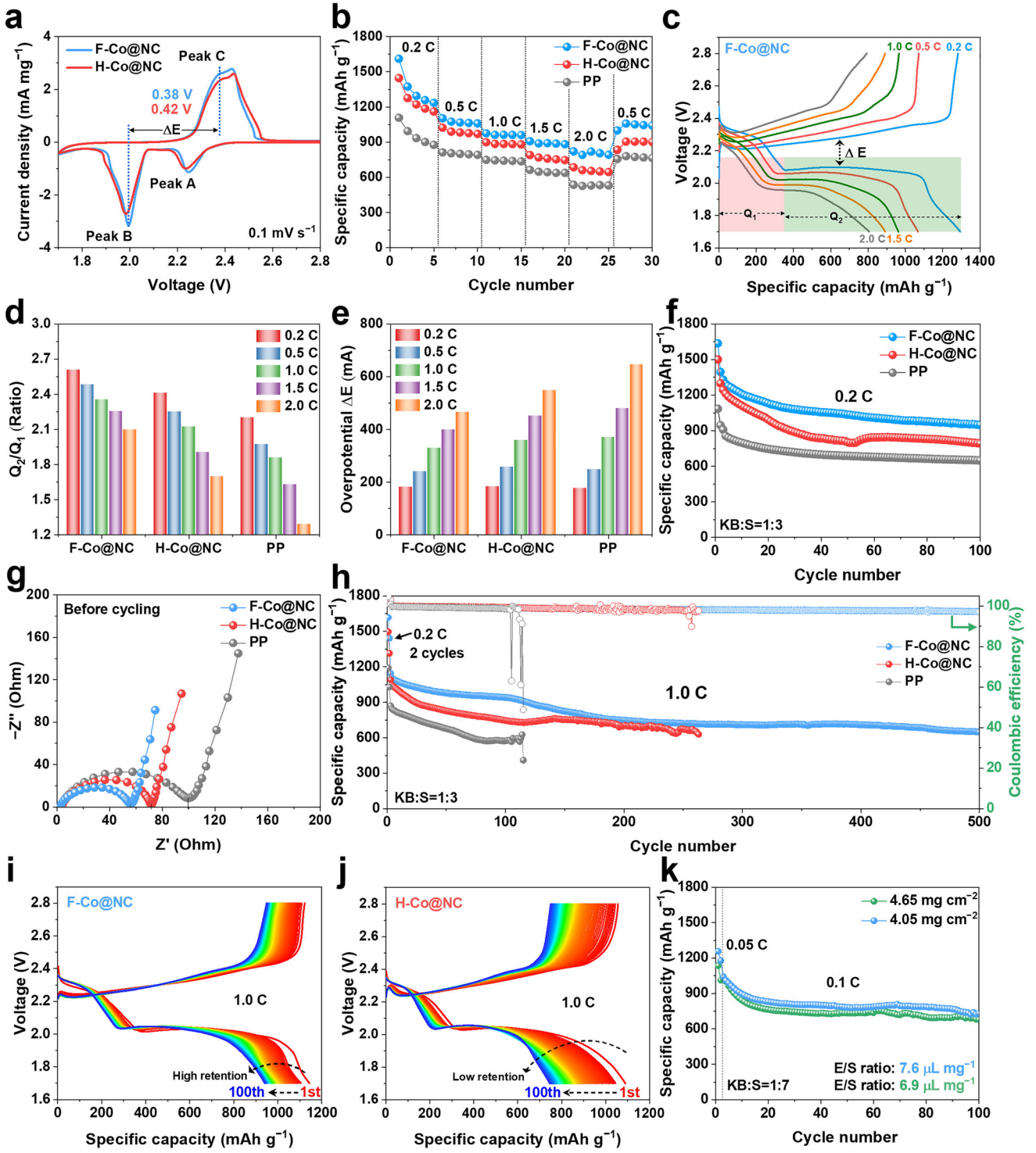

Figure 4. a) CV curves of the cells with F-Co@NC and H-Co@NC at a scan rate of 0.1 mV s^{-1}. b) Rate capability of the cells under various current rates. c) Galvanostatic charge–discharge profiles of the cell with F-Co@NC under various current rates. Comparison of d) Q_2/Q_1, and e) the overpotential values. f) Cycling performance of the cells at 0.2 C for 100 cycles. g) Nyquist plots of the cells before cycling. h) Cycling performance of the cells at 1.0 C. Galvanostatic charge–discharge profiles of the cells with i) F-Co@NC and j) H-Co@NC during the 100 cycles at 1.0 C. k) Cycling performance of the cells with F-Co@NC with sulfur loadings of 4.05 and 4.65 mg cm^{-2} at 0.1 C.

37.9%. The high specific capacity and sulfur utilization of the cell with F-Co@NC suggest that its superior electrocatalytic activity enhances redox reversibility by facilitating the conversion of LiPSs and effectively suppressing their shuttling effect. Electrochemical impedance spectroscopy (EIS) measurements were carried out to evaluate the influence of F-Co@NC and H-Co@NC on charge transfer behavior within the cell. As shown in Figure 4g, the EIS spectra of fresh cells consisted of one semicircle at high to medium frequencies and one inclined line at low frequencies. The starting point of the semicircle represents the bulk resistance (R_b) derived from the ion migration within the electrolyte, the semicircle corresponds to the charge transfer resistance (R_{ct}), and the inclined line is associated with the Warburg impedance (W) related to diffusion of Li^+ into the sulfur cathode.[79] The equivalent circuits employed to analyze the EIS are presented in Figure S29 (Supporting Information). Compared to the cells with H-Co@NC and PP, the R_{ct} of the cell with F-Co@NC was lower, indicating the improved interfacial charge transfer of the cell with F-Co@NC (Table S5, Supporting Information). In addition, the EIS spectra of cells after 100 cycles were also investigated (Figure S30, Supporting Information). A new semicircle appearing in the EIS spectra after cycling represents the solid electrolyte interphase (SEI) layer resistance (R_{SEI}), associated with the formation of solid Li_2S_2 and Li_2S. The corresponding equivalent circuits are presented in Figure S31 (Supporting Information). After 100 cycles, the F-Co@NC cell exhibited the lowest R_{ct} and R_{SEI} values compared to the H-Co@NC and PP cells. This result could be attributed to the fact that F-Co@NC not only retained its capability to accelerate charge transfer, but also effectively alleviated the undesirable accumulation of electrically resistive Li_2S_2/Li_2S layer during prolonged cycling. Moreover, we verified that the R_b values for the F-Co@NC cell were lower than those for the H-Co@NC and PP cells. This improvement can be ascribed to the mitigated LiPS shuttling, which prevented the increase in electrolyte viscosity that could hinder ion mobility. The corresponding R_b, R_{SEI}, and R_{ct} values are listed in Table S6 (Supporting Information).

Although the cell with F-Co@NC exhibited stable cycling with high specific capacity under mild current conditions, LSBs still face significant challenges at high current densities due to the sluggish redox reactions of poorly conductive solid-phase LiPSs. As such, we further investigated the long-term cycling behavior at high current densities. As demonstrated in Figure 4h, the cell with F-Co@NC demonstrated stable cycling over 500 cycles at a current density of 1.0 C, maintaining a specific capacity of 648.5 mAh g^{-1}. In comparison, the cell with H-Co@NC demonstrated unstable cycling behavior after 250 cycles, and the cell with PP separator showed catastrophic cell failure after 110 cycles. The GCD profiles of each cell were analyzed to gain deeper insight into the charge/discharge behavior at high current density. As shown in Figure 4i, the GCD profiles of the F-Co@NC cell were well-maintained during the 100 cycles, retaining its superior LiPSs reduction efficiency. The specific capacity of the cell with F-Co@NC after 100 cycles was 938.9 mAh g^{-1}, and the cell also demonstrated high capacity retention of 82%. In contrast, the cell with H-Co@NC and PP separator exhibited lower specific capacities of 742.2 and 577.9 mAh g^{-1}, respectively, and the cell with H-Co@NC retained only 68% of its initial capacity (Figure 4j; Figure S32, Supporting Information). Furthermore, even at a higher current density of 2.0 C, the F-Co@NC cell retained a specific capacity of 668.3 mAh g^{-1} after 245 cycles, with a low capacity decay of 0.13% per cycle (Figure S33, Supporting Information). These results demonstrate that F-Co@NC, with its superior charge transfer capability, enables long-term stable cycling under high charge/discharge rates by facilitating the redox reactions of LiPSs and alleviating their shuttling effect. A comprehensive comparison of recently reported studies is summarized in Table S9 (Supporting Information), demonstrating the superior rate capability and cycling stability of the F-Co@NC cell compared with previous reports.

To better clarify the effects of cobalt incorporation and phase regulation, a comprehensive evaluation of the electrochemical performance of cells with a cobalt-free nitrogen-doped carbon (denoted as NC) coated separator was conducted. The electrochemical performances of the cells with NC were superior compared to the cells with PP. However, cells with F-Co@NC and H-Co@NC delivered larger specific capacity and demonstrated improved long-term cycling stability (Figures S34–S36, Supporting Information). These findings suggest that the incorporation of cobalt into the carbon shells and its ability to modulate the electronic structures of the carbon shells further enhance the electrochemical performances of the LSBs. The detailed discussion and electrochemical performance comparison of the cells with NC are presented in the supporting information and Tables S7 and S8 (Supporting Information).

Enabled by its ability to promote the redox reactions of LiPSs, the cell with F-Co@NC delivered superior electrochemical performance even under high sulfur loadings (Figure 4k). After 100 cycles, the cell with a sulfur loading of 4.05 mg cm^{-2} retained a specific capacity of 731.5 mAh g^{-1} at 0.1 C with a capacity decay of 0.30% per cycle. When the sulfur loading was increased to 4.65 mg cm^{-2}, the cell still delivered a specific capacity of 679.5 mAh g^{-1} after 100 cycles, with a low capacity decay of 0.34% per cycle. Additionally, we confirmed that the GCD profiles of the cells with sulfur loadings of 4.05 and 4.65 mg cm^{-2} were stable, indicating that F-Co@NC contributes to maintaining favorable LiPSs redox reversibility under high sulfur loading conditions (Figure S37, Supporting Information). Considering that the commercial Li-ion batteries (LIBs) typically deliver an areal capacity of ≈4 mAh cm^{-2}, we further increased the sulfur loading to assess the cathode requirement for surpassing this benchmark. As shown in Figure S38 (Supporting Information), the F-Co@NC-based cell exhibited and sustained an areal capacity exceeding that of commercial LIBs with a sulfur loading of 5.18 mg cm^{-2} during 50 cycles, reaffirming the superior redox reaction and mitigated shuttling behavior of LiPSs enabled by the F-Co@NC. After confirming the favorable electrocatalytic performance of F-Co@NC with higher sulfur contents, we fabricated a soft-packed cell to verify the compatibility of F-Co@NC-modified separator under an enlarged electrode area. As illustrated in Figure S39 (Supporting Information), the soft-packed cell with F-Co@NC showed stable GCD profiles with a reasonable specific capacity and was able to power an LED array, demonstrating its reliable electrochemical operation. These notably enhanced electrochemical performances of the LSBs with F-Co@NC suggest that regulating the crystalline phase of the cobalt embedded within the carbon shell can be an effective strategy to improve

the catalytic effects of cobalt-integrated carbon–metal composite electrocatalysts.

Through comprehensive electrochemical analyses, we confirmed that although the heteroatom doping content of F-Co@NC was lower than that of H-Co@NC, the cells with F-Co@NC demonstrated superior electrochemical performance. Considering that a higher level of heteroatom doping is generally beneficial for facilitating LiPSs conversion and mitigating the shuttling effect, the superiority of the cells with F-Co@NC implies that the modulation of the electronic properties of F-Co@NC through the phase transition of cobalt from HCP to FCC provides a significant catalytic advantage to cobalt–carbon catalysts, compensating for and even surpassing the reduction in doping.[80–84] Motivated by this interpretation, to understand the underlying reasons for the superior electrochemical performance of the cells with F-Co@NC, we systematically explored the redox kinetics and electrocatalytic behaviors associated with the crystalline phase of cobalt. As shown in the contour plots of CV profiles at different scan rates, the cell with F-Co@NC exhibited a larger current response in both cathodic and anodic reactions and narrower potential regions associated with the reduction of soluble LiPSs to solid Li_2S_2/Li_2S and the oxidation of solid Li_2S, compared to the cell with H-Co@NC. These results indicate the accelerated redox kinetics of the cell with F-Co@NC, which could be attributed to the facile electronic and ionic transport provided by F-Co@NC (**Figure 5a,b**). To evaluate the diffusion behavior of Li^+ during the redox reaction, peaks in the CV curves at various scan rates were further investigated (Figure 5c; Figure S40, Supporting Information). Li^+ diffusion efficiency was assessed based on the Randles–Sevcik Equation (2):

$$I_p = \left(2.69 \times 10^5\right) n^{1.5} S D_{Li+}^{0.5} C_{Li+} \nu^{0.5} \tag{2}$$

in which I_p denotes the peak current, n is the number of electrons transferred ($n = 2$), S is the geometric area of the active electrode (1.13 cm^2), D represents the diffusion coefficient of Li^+, C is the Li^+ concentration in the cathode (0.001 mol mL^{-1}), and ν is the scan rate of potential. Since n, S, C, and ν are predetermined, I_p is linearly proportional to $V^{1/2}$ $s^{-1/2}$. Thus, the slope of the I_p–$V^{1/2}$ $s^{-1/2}$ plot is directly correlated with the Li^+ diffusion coefficient D, and the linear relationships between I_p and $V^{1/2}$ $s^{-1/2}$ are presented in Figure 5d and Figure S41 (Supporting Information). As depicted in Figure 5e, the F-Co@NC exhibited steeper slopes than H-Co@NC across all four peaks in the I_p–$\nu^{1/2}$ plots, suggesting that F-Co@NC enables fast Li^+ migration during both discharge and charge processes. These findings align well with the computational simulation presented earlier.

During the reduction process, conversion from Li_2S_4 to Li_2S_2/Li_2S is recognized as the rate-limiting step due to its high energy barrier.[85,86] Thus, the ability of the electrocatalyst to accelerate this key transformation is crucial. To evaluate the effect of F-Co@NC on the activation energy associated with this step, we carried out temperature-dependent EIS analysis after generating Li_2S_4 by pre-discharging the cell to 2.1 V, and corresponding R_{ct} values were obtained (Figure S42, Supporting Information).[87,88] A linear relationship was observed when plotting $\ln(1/R_{ct})$ against the inverse absolute temperature ($1/T$), consistent with the Arrhenius formula Equation (3):

$$\frac{1}{R_{ct}} = A exp\left(-\frac{E_a}{RT}\right) \tag{3}$$

where A is the pre-exponential factor, E_a is the activation energy for the reduction process of Li_2S_4, R is the ideal gas constant (8.314 J $(mol{\cdot}K)^{-1}$), and T is the absolute temperature. As shown in Figure S43 (Supporting Information), the cell with F-Co@NC exhibited a lower activation energy (18.92 kJ mol^{-1}) than that with H-Co@NC (22.49 kJ mol^{-1}), indicating that F-Co@NC more effectively promotes the liquid-to-solid conversion of Li_2S_4 during discharge. This result is also in line with previous theoretical calculations and further supports the high reduction efficiency confirmed in the electrochemical performance analysis.

Improving the redox kinetics of liquid LiPSs is essential not only for achieving superior electrochemical performance but also for suppressing the shuttle effect by narrowing the time window for LiPSs diffusion from cathode to anode.[89] In this context, comprehensive investigations were conducted using Li_2S_6-based symmetric cells to assess the electrocatalytic behavior of F-Co@NC and H-Co@NC toward soluble LiPSs. As displayed in Figure 5f, the symmetric cell incorporating F-Co@NC showed a reduced charge transfer resistance relative to H-Co@NC, indicating the rapid electron conduction between F-Co@NC and Li_2S_6. Subsequently, the CV analysis was performed at a slow scan rate of 1 mV s^{-1} to thoroughly evaluate their catalytic effects on the reversible conversion of LiPSs. As illustrated in Figure 5g, two pairs of redox peaks were observed in both CV profiles, arising from the stepwise redox processes of Li_2S_6. During the cathodic scan, peaks A and B arise from the sequential reduction of S_8 to Li_2S_6 and further to Li_2S at the working electrode. In the subsequent anodic scan, peaks C and D correspond to the oxidation of Li_2S to Li_2S_6 and then to S_8 at the working electrodes.[90,91] Counter electrode reactions proceeded concurrently to complete the redox cycle and ensure charge compensation. We verified that all redox peaks of the symmetric cell with F-Co@NC appeared with higher intensities and smaller overpotentials compared to those with H-Co@NC. Furthermore, the cell with F-Co@NC retained well-defined pairs of redox peaks even at a scan rate of 10 mV s^{-1}, whereas those of the cell with H-Co@NC became broadened and less distinguishable (Figure S44, Supporting Information). These results highlight the superior electrocatalytic performance of F-Co@NC with faster reaction kinetics and enhanced redox reversibility. The enhanced electrocatalytic capability of F-Co@NC for the conversion of LiPSs was further revealed by Tafel analysis conducted within the overpotential range from −70 to 70 mV. As shown in Figure 5h, the cell with F-Co@NC showed a notably higher exchange current density (5.36×10^{-2} mA cm^{-2}) compared to that with H-Co@NC (2.26×10^{-2} mA cm^{-2}) in both the reduction and oxidation processes, reflecting its faster interfacial electron transfer rate. In addition, chronoamperometry measurements provided further insight into the catalytic behavior of F-Co@NC and H-Co@NC. As presented in Figure 5i, a negligible current response was observed in the absence of Li_2S_6, confirming that the recorded current originates from the redox conversion of LiPSs. Upon addition of Li_2S_6, the cell with F-Co@NC exhibited a higher and more sustained current response compared

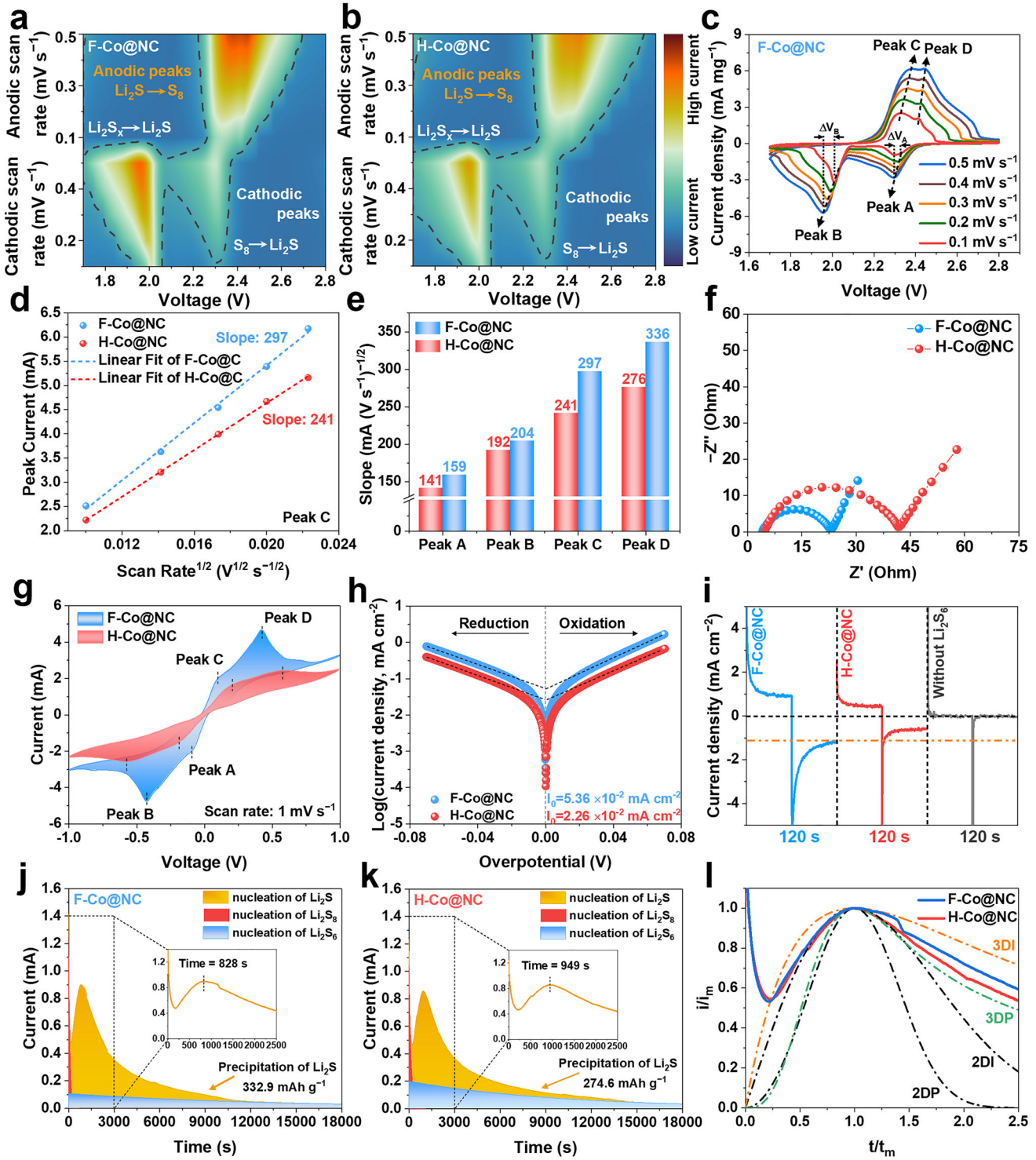

Figure 5. Contour plots for the CV profiles of a) F-Co@NC and b) H-Co@NC. c) CV profiles of the cell with F-Co@NC at various scan rates. d) Linear relationship between peak current of Peak C and the square root of scan rate. e) Comparison of slopes from the linear fitting of peak current versus the square root of scan rate for Peaks A–D. f) Nyquist plots of the symmetric cells. g) CV profiles of Li_2S_6 symmetric cells at a scan rate of 1 mV s^{-1}. h) Tafel plots and i) Chronoamperometric curves of Li_2S_6 symmetric cells. Potentiostatic discharge profiles at 2.05 V on j) F-Co@NC and k) H-Co@NC with Li_2S_8. l) Dimensionless transient plots of the cells with theoretical growth models.

to the H-Co@NC-based cell, further corroborating the superior catalytic activity of F-Co@NC in promoting the redox conversion of LiPSs.

The transformation from soluble LiPSs to solid-state Li_2S plays a pivotal role in achieving a high capacity of LSBs. However, the inherently low electrical conductivity of the solid discharge product severely impedes their continuous formation. Thus, to evaluate the effect of the enhanced interfacial charge transfer capability of F-Co@NC, achieved through the regulation of the cobalt crystalline phase, on the sustained conversion behavior of Li_2S_4 to solid Li_2S_2/Li_2S, a Li_2S nucleation test was conducted. As illustrated in Figure 5j,k, the capacity derived from the precipitation of Li_2S on F-Co@NC (332.9 mAh g^{-1}) significantly surpassed that on H-Co@NC (274.6 mAh g^{-1}). Besides, the peak current associated with Li_2S deposition was observed earlier on F-Co@NC (828 s) than on H-Co@NC (949 s), and the calculated Li_2S nucleation rate constant was significantly higher for F-Co@NC (11.21×10^{-10} S^{-3}) than for H-Co@NC (7.44×10^{-10} S^{-3}) (Figure S45, Supporting Information).[92] These results clarify that the enhanced electron transport capability of F-Co@NC accelerates the sluggish nucleation and growth of Li_2S, thereby increasing both the amount and rate of solid-phase Li_2S formation. The favorable formation of Li_2S on F-Co@NC was further supported by employing the nucleation model based on the Scharifker–Hills theory.[93] As depicted in Figure 5l, both F-Co@NC and H-Co@NC were located between the theoretical curves for the 3D instantaneous (3DI) and progressive (3DP) nucleation. We verified that the profile of F-Co@NC was relatively closer to the 3DI model than H-Co@NC, suggesting that Li_2S nucleation on F-Co@NC proceeds more rapidly and uniformly across active sites. This behavior is indicative of the stronger catalytic activity of F-Co@NC, which originates from its effective interfacial electron transport capability.

While the nucleation of Li_2S is crucial for the discharge process in LSBs, its subsequent decomposition during the charging process should also be carefully considered, as it governs the reversibility of sulfur redox reactions. Accordingly, the dissociation behavior of Li_2S was also investigated (Figure S46, Supporting Information). Similar to the Li_2S nucleation behavior, F-Co@NC exhibited a greater capacity derived from the decomposition of Li_2S than H-Co@NC, along with a shorter time to reach the peak current. The corresponding Li_2S dissociation rate, calculated from the time required to reach the peak current, was determined to be 2.38×10^{-10} S^{-3} for F-Co@NC, which is more than twice that of H-Co@NC (1.10×10^{-10} S^{-3}) (Figure S47, Supporting Information). This result further demonstrates that F-Co@NC facilitates not only the rapid formation but also the efficient dissociation of Li_2S, highlighting its bidirectional catalytic activity toward both the reduction and oxidation processes of Li_2S.

From previous results, F-Co@NC exhibits excellent electrocatalytic activity in promoting the redox kinetics of LiPSs, which could explain the superior electrochemical performance of the LSBs with F-Co@NC. However, to fully leverage this catalytic effect over prolonged cycling, it is crucial to mitigate the loss of active sulfur caused by the shuttle behavior of LiPSs. As such, the ability of the electrocatalyst to effectively anchor LiPSs and mitigate its shuttling behavior is also a key factor in improving the long-term cycling performance of LSBs. To experimentally validate the superior LiPSs adsorption capability of F-Co@NC predicted by the theoretical calculations, the same weight of F-Co@NC and H-Co@NC (10 mg) was immersed in a 25 mM Li_2S_6 solution, and the corresponding color changes were observed (**Figure 6a**). As shown in Figure 6b and F-Co@NC significantly decolorized the Li_2S_6 solution compared to H-Co@NC, indicating its superior Li_2S_6 anchoring capability. The visually observed differences in the Li_2S_6 solutions were further quantified by UV–vis spectroscopy (Figure 6c). Before conducting the analysis, each Li_2S_6 solution was diluted to 12.5 mM to minimize the influence of the precipitated F-Co@NC and H-Co@NC particles at the bottom of the vial during sample extraction. Interestingly, we verified that the Li_2S_6 solution with H-Co@NC slightly decolorized only after dilution, revealing its relatively weak LiPSs adsorption ability compared to F-Co@NC, which had been barely discernible at the 25 mM Li_2S_6 solution (inset of Figure 6c). The significantly reduced peak intensity of the Li_2S_6 solution with F-Co@NC, compared to the pure Li_2S_6 solution and Li_2S_6 solution with H-Co@NC, further demonstrates the strong LiPSs anchoring capability of F-Co@NC. Subsequently, to examine the effect of strong LiPSs anchoring on the suppression of LiPSs shuttling behavior, a permeation test was carried out using H-shaped glass cells. The two chambers, containing 0.5 M Li_2S_6 solution (left chamber) and pure electrolyte (right chamber), respectively, were partitioned by either F-Co@NC- or H-Co@NC-coated separator. As shown in Figure 6d, the solution in the right chamber of the H-shaped cell, separated by the F-Co@NC-coated separator, retained a slightly yellow but transparent appearance even after 24 h. In comparison, the solution in the right chamber of the cell with H-Co@NC-coated separator gradually turned dark brown and lost its transparency over time (Figure S48, Supporting Information). These results indicate that the F-Co@NC-coated layer, which strongly captures LiPSs, serves as an effective barrier against the permeation of LiPSs, which could suppress the shuttling behavior of LiPSs in LSBs.

Through comprehensive liquid-phase LiPSs adsorption tests excluding LiPSs conversion processes, we verified that F-Co@NC exhibits stronger LiPSs adsorption than H-Co@NC. Subsequently, to evaluate the effect of the strong LiPSs migration resistance provided by F-Co@NC under electrochemical environments, the self-discharge behavior of LSBs was first investigated. As shown in Figure S49 (Supporting Information), after charging to 2.8 V, the cell with a PP separator suffered a severe drop in open-circuit voltage (OCV) over time, suggesting the unrestrained diffusion of LiPSs from the cathode to the anode due to the lack of an adsorption barrier. In contrast, the OCV of both F-Co@NC and H-Co@NC cells remained stable without an abrupt decline. Especially, the F-Co@NC cell maintained a higher OCV than the H-Co@NC cell, indicating that F-Co@NC with high LiPSs adsorption capability effectively mitigated the shuttling behavior of LiPSs. The superior suppression of LiPSs shuttling by F-Co@NC was further supported by a leakage current test. Both F-Co@NC and H-Co@NC cells were discharged to 2.38 V to generate soluble LiPSs, followed by a constant-voltage hold at 2.38 V. As shown in Figure 6e, the cell with F-Co@NC demonstrated a lower leakage current, attributed to reduced migration of LiPSs toward the anode. This result further clarifies the superior capability of F-Co@NC to alleviate LiPSs shuttling. To provide a more intuitive assessment of the adsorption capability

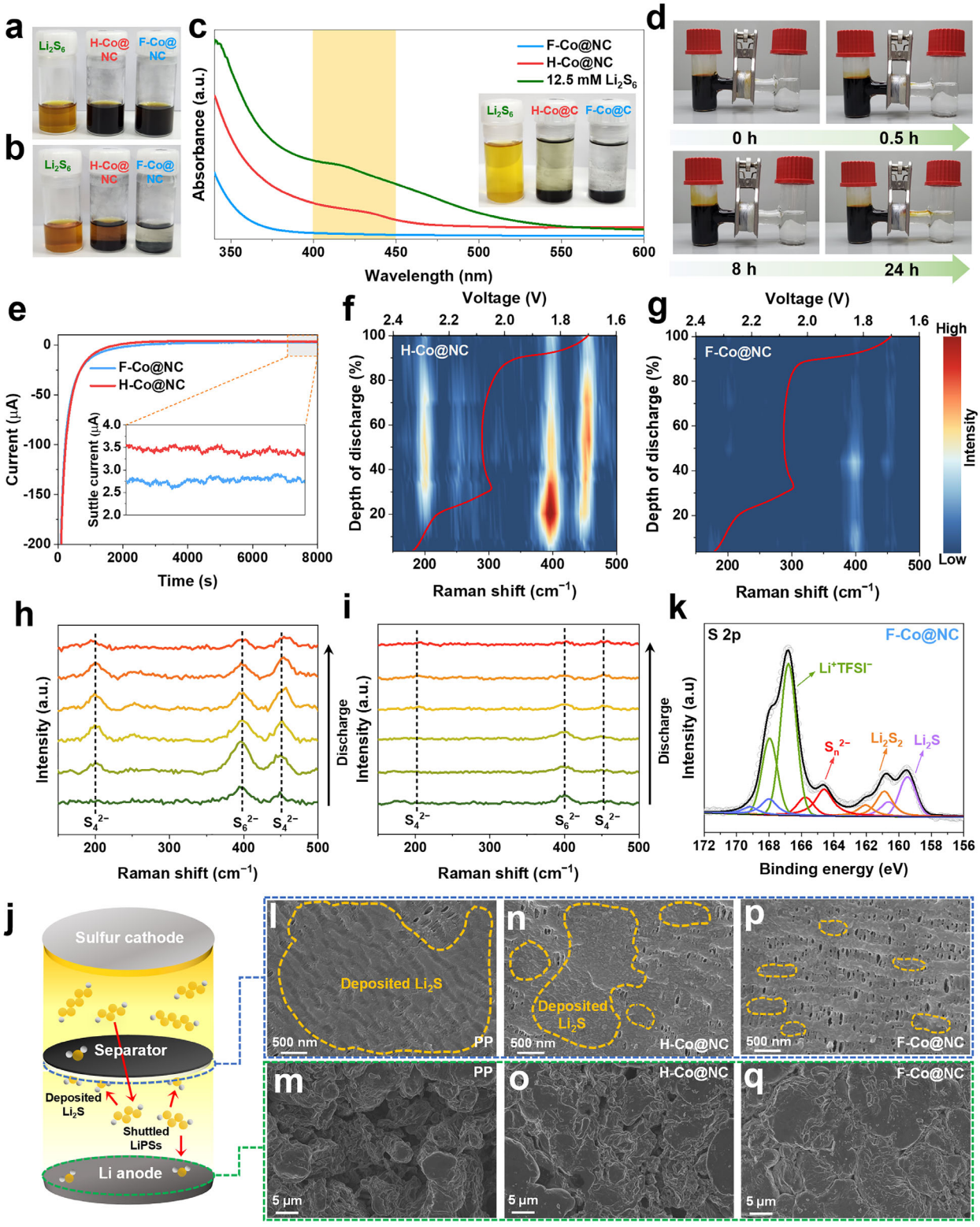

Figure 6. Photographic images of the blank 25.0 mM Li_2S_6 solutions and their static adsorption by F-Co@NC and H-Co@NC: a) immediately after catalyst introduction, and b) after 24 h. c) UV–vis spectra of 12.5 mM Li_2S_6 solutions after interaction with F-Co@NC and H-Co@NC. d) Permeation test of Li_2S_6 using H-type cells with an F-Co@NC-coated separator. e) Shuttle currents of the cells. In situ Raman spectra and corresponding contour maps of the cells with f,h) H-Co@NC and g,i) H-Co@NC. j) Schematic illustration of the shuttling pathway of LiPSs in LSBs. k) XPS spectra of S 2p for the F-Co@NC coating layer after cycling. SEM images of the anode-facing side of separators and lithium metal anode after cycling in cells with l,m) PP, n,o) H-Co@NC, and p,q) F-Co@NC.

and electrocatalytic performance of F-Co@NC and H-Co@NC, we implemented in situ Raman spectroscopy to track the behavior of dissolved liquid LiPSs species in real time.[94–96] As displayed in Figure 6f,h, the cell with H-Co@NC exhibited clear bands attributable to S_6^{2-} (≈400 cm^{-1}) and S_4^{2-} (≈200 and ≈ 450 cm^{-1}) during discharge, and these signals persisted to the end of discharge. In contrast, in the cell with F-Co@NC, the intensities of LiPSs-related bands were consistently lower throughout discharge and decreased progressively as discharge proceeded (Figure 6g,i). These observations support that F-Co@NC effectively suppresses LiPSs shuttling and accelerates its conversion.

To gain deeper insights into the influence of F-Co@NC on the integrity of key components in LSBs, including the separator and lithium metal anode, during repeated charge and discharge processes, a series of investigations was conducted on cycled cells along the shuttling pathway of LiPSs within the cell (Figure 6j). Ex situ XPS analysis was conducted on the cathode-facing side of the separator, where migrating LiPSs initially come into contact (Figure 6k; Figure S50, Supporting Information). The S 2p spectra were deconvoluted into four pairs of doublets, and the corresponding S $2p_{3/2}$ peaks were assigned to the LiTFSI in the electrolyte (168.0 and 166.8 eV), Li_2S_x ($x \geq 4$) (164.6 eV), Li_2S_2 (160.9 eV), and Li_2S (159.5 eV), respectively. Both F-Co@NC and H-Co@NC coating layers showed higher intensities of LiPSs-derived peaks compared to the PP separator, indicating their ability to adsorb LiPSs. Notably, the intensities of the solid-phase Li_2S_2 and Li_2S peaks on the F-Co@NC coating layer were higher than those on the H-Co@NC coating layer. These results imply that F-Co@NC more effectively restricts the loss of sulfur active materials toward the anode side, enabling their effective reutilization on the cathode side. Subsequently, XPS analysis on the cycled lithium metal anodes was also performed to examine the shuttled LiPSs to the lithium metal anode. The S 2p spectra were deconvoluted into four pairs of peaks at 160.9 and 159.5 eV, corresponding to the S $2p_{3/2}$ peaks of Li_2S_2 and Li_2S, respectively.[97] As shown in Figure S51 (Supporting Information), the lithium metal anode from the F-Co@NC cell exhibited lower intensities of LiPSs-derived components than those from H-Co@NC and PP separator cells, indicating reduced LiPSs deposition and anode corrosion, which is attributed to the effective mitigation of LiPSs shuttling. To explore the influence of shuttled LiPSs permeating through the separator on the anode side of the cell, morphological investigations were performed using SEM on both the anode-facing side of the separator and the surface of the lithium metal anode. SEM images of the pristine PP separator and lithium metal were first examined (Figures S52 and S53, Supporting Information). We confirmed that the pristine PP separator exhibited a highly porous structure. In parallel, the pristine lithium metal displayed a smooth and uniform surface. As shown in Figure 6i, the anode-facing side of the separator retrieved from the PP-based cell displayed numerous blocked pores, attributed to the substantial accumulation of solid-phase LiPSs due to the shuttling of soluble LiPSs species. Concurrently, the lithium metal surface of the cell with the PP separator also exhibited a severely roughened and non-uniform morphology, suggesting that the substantial deposition of LiPSs on the lithium metal anode disrupted the uniform lithium plating and stripping behavior and induced parasitic reactions during cycling (Figure 6j). Compared to PP, the separator coated with H-Co@NC showed fewer blocked pores (Figure 6k). Nevertheless, notable LiPSs deposition on the separator and degradation of the lithium metal surface were still observed (Figure 6l). In contrast, the anode-facing side of the F-Co@NC-coated separator retained a significantly more open pore structure (Figure 6m). Furthermore, the lithium metal surface remained smooth with high grain-to-grain connectivity (Figure 6n). These results indicate that the F-Co@NC coating effectively suppresses the shuttling of LiPSs toward the anode during repeated cycling. Therefore, the strong LiPSs anchoring ability of F-Co@NC not only sustains high sulfur utilization but also preserves the integrity of the lithium metal anode, ultimately contributing to the significantly improved electrochemical performance of LSBs. To address the potential phase transition from FCC to HCP during extended cycling, we performed XRD analysis on the F-Co@NC-modified separator before and after 245 cycles at 2.0 C. We found that the FCC phase cobalt in F-Co@NC was well-retained, with details provided in Figures S54 and S55 (Supporting Information).

In this study, crystallographic control of cobalt within the cobalt–carbon composite not only accelerates LiPSs conversion but also mitigates the LiPSs shuttling. Beyond cobalt–carbon, this crystallographic engineering concept could be readily generalized to other metal–carbon composite systems, including iron–carbon, nickel–carbon, and manganese–carbon. By systematically tuning the crystal phase of the metal core, the sequence of transformation steps that encompass adsorption and interfacial charge transfer can be improved, enabling performance enhancements not only in LSBs but also across other conversion-type batteries. In particular, extending this framework to Li–O_2, Na–S, and Zn–air systems, where multielectron conversion and phase transformation govern reactivity, could help establish generalizable design rules for catalysts and electrodes in next-generation systems.

3. Conclusion

In summary, this study demonstrated that crystalline phase engineering of cobalt nanoparticles encapsulated within a carbon shell constitutes an effective route to enhancing the intrinsic catalytic activity of metal–carbon electrocatalysts for LSBs. Transitioning cobalt from the HCP to the FCC phase elevates the interfacial potential gradient, thereby intensifying electron transfer to the carbon shell and significantly enriching the electronic density near the E_F. This phase-induced modulation of the carbon shell's electronic band structure not only accelerates the bidirectional conversion of LiPSs but also strengthens the chemisorption of LiPSs, leading to enhanced redox reversibility and suppressed shuttling behavior of LiPSs. Consequently, the cell with F-Co@NC delivers improved rate capability and long-term cycling stability, maintaining high sulfur utilization and the integrity of the lithium metal anode. Beyond its immediate performance benefits, this work establishes a universally applicable and mechanistically grounded design strategy, which is able to operate synergistically with approaches aimed at increasing the catalytically active surface area, thereby offering fundamental guidance for the rational design strategy of metal–carbon composite catalysts for various next-generation energy storage systems requiring multi-electron reactions.

4. Experimental Section

Synthesis of F-Co@NC and H-Co@NC: To prepare the homogeneous precursor comprising carbon and cobalt, a plasma engineering method was applied to the mixture of pyridine and cobalt hexahydrate in DMF, following a previously reported procedure.[40,41] Then, the precursor was annealed at 700 °C in a nitrogen atmosphere, with a heating rate of 2 °C min^{-1} from room temperature and without any holding time. After natural cooling to ≈40 °C in the furnace, the resulting powders were collected and finely ground to obtain F-Co@NC. The H-Co@NC sample was prepared following the same procedure but at an annealing temperature of 600 °C.

Fabrication of F-Co@NC and H-Co@NC Modified Separators: To fabricate the F-Co@NC-modified separator, F-Co@NC, Super P (Alfa Aesar), and Polyvinylidene fluoride (PVDF, Wellcos) were mixed at a weight ratio of 8:1:1 and dispersed in N-methyl-2-pyrrolidone (NMP, Sigma–Aldrich). The mixture was then homogenized using a paste mixer (ARV-310) at 1500 rpm for 1 h. The slurry was coated on a polypropylene (PP) separator (Celgard 2400, Wellcos) and dried at 50 °C for 24 h under vacuum. The resulting F-Co@NC-modified separator was shaped into discs with a 19 mm diameter. The H-Co@NC-modified separator was fabricated in the same manner. The loading mass of the F-Co@NC and H-Co@NC was ≈ 0.5 mg cm^{-2}.

Supporting Information

Supporting Information is available from the Wiley Online Library or from the author.

Acknowledgements

This work was supported by the 2024 BK21 FOUR Graduate School Innovation Support funded by Pusan National University (PNU-Fellowship program). This research was supported by the Nano & Material Technology Development Program through the National Research Foundation of Korea (NRF), funded by the Ministry of Science and ICT (50%, RS-2025-25441820), the National Research Council of Science & Technology (NST) grant by the Korea government (MSIT) (15%, No. GTL24012-000), the National Research Foundation of Korea (NRF) grant funded by the Korea government (Ministry of Science and ICT) (20%, No. RS-2025-02315340). This work was also financially supported by grants from the National Research Foundation of the Republic of Korea, funded by the Ministry of Education (15%, Grant No. RS-2025-25415557).

Conflict of Interest

The authors declare no conflict of interest.

Author Contributions

J.-O.K., H.G. and S.K. contributed equally to this work. J.-O.K. contributed to the conceptualization, carried out the experimental investigations, and wrote the original draft. H.G. performed the DFT calculations. S.K. synthesized the precursors and conducted experimental investigations. J.B.P., S.C., T.K., S.H., G.A.D.L.G.G. M.P. and J.H.K. assisted in conducting experimental investigations. O.L.L., S.G.L., and J.H.L. proposed the research concept, supervised the work, and contributed to the review and editing of the draft. All authors discussed the results and commented on the manuscript.

Data Availability Statement

The data that support the findings of this study are available from the corresponding author upon reasonable request.

Keywords

catalytic conversion, crystalline phase engineering, electrocatalyst, interfacial potential gradient, lithium–sulfur batteries

Received: September 23, 2025
Revised: November 3, 2025
Published online: November 22, 2025

[1] X.-Y. Li, S. Feng, Y.-W. Song, C.-X. Zhao, Z. Li, Z.-X. Chen, Q. Cheng, X. Chen, X.-Q. Zhang, B.-Q. Li, J.-Q. Huang, Q. Zhang, *J. Am. Chem. Soc.* **2024**, *146*, 14754.
[2] X. Ji, K. T. Lee, L. F. Nazar, *Nat. Mater.* **2009**, *8*, 500.
[3] G. Zhou, H. Chen, Y. Cui, *Nat. Energy* **2022**, *7*, 312.
[4] X. Yang, J. Luo, X. Sun, *Chem. Soc. Rev.* **2020**, *49*, 2140.
[5] Q. Pang, X. Liang, C. Y. Kwok, L. F. Nazar, *Nat. Energy* **2016**, *1*, 16132.
[6] J. Wu, T. Ye, Y. Wang, P. Yang, Q. Wang, W. Kuang, X. Chen, G. Duan, L. Yu, Z. Jin, J. Qin, Y. Lei, *ACS Nano* **2022**, *16*, 15734.
[7] W. Xiao, K. Yoo, J. Kim, H. Xu, *ACS Nano* **2024**, *18*, 32732.
[8] Z. Du, X. Chen, W. Hu, C. Chuang, S. Xie, A. Hu, W. Yan, X. Kong, X. Wu, H. Ji, L. J. Wan, *J. Am. Chem. Soc.* **2019**, *141*, 3977.
[9] Q. Yang, J. Cai, G. Li, R. Gao, Z. Han, J. Han, D. Liu, L. Song, Z. Shi, D. Wang, G. Wang, W. Zheng, G. Zhou, Y. Song, *Nat. Commun.* **2024**, *15*, 3231.
[10] H. Cheng, Z. Shen, W. Liu, M. Luo, F. Huo, J. Hui, Q. Zhu, H. Zhang, *ACS Nano* **2023**, *17*, 14695.
[11] Q. Zeng, L. Xu, G. Li, Q. Zhang, S. Guo, H. Lu, L. Xie, J. Yang, J. Weng, C. Zheng, *Adv. Funct. Mater.* **2023**, *33*, 2304619.
[12] Z. Han, S. Zhao, J. Xiao, X. Zhong, J. Sheng, W. Lv, Q. Zhang, G. Zhou, H.-M. Cheng, *Adv. Mater.* **2021**, *33*, 2105947.
[13] Y. Song, W. Cai, L. Kong, J. Cai, Q. Zhang, J. Sun, *Adv. Energy Mater.* **2020**, *10*, 1901075.
[14] Z. Wu, M. Liu, W. He, T. Guo, W. Tong, E. Kan, X. Ouyang, F. Qiao, J. Wang, X. Sun, X. Wang, J. Zhu, A. Coskun, Y. Fu, *Nat. Commun.* **2024**, *15*, 9535.
[15] X. Liang, C. Hart, Q. Pang, A. Garsuch, T. Weiss, L. F. Nazar, *Nat. Commun.* **2015**, *6*, 5682.
[16] Q. Pang, D. Kundu, M. Cuisinier, L. F. Nazar, *Nat. Commun.* **2014**, *5*, 4759.
[17] S. Deng, T. Guo, J. Heier, C. J. Zhang, *Adv. Sci.* **2023**, *10*, 2204930.
[18] R. Wang, C. Luo, T. Wang, G. Zhou, Y. Deng, Y. He, Q. Zhang, F. Kang, W. Lv, Q. H. Yang, *Adv. Mater.* **2020**, *32*, 2000315.
[19] J. B. Zhou, X. J. Liu, L. Q. Zhu, J. Zhou, Y. Guan, L. Chen, S. W. Niu, J. Y. Cai, D. Sun, Y. C. Zhu, J. Du, G. M. Wang, Y. T. Qian, *Joule* **2018**, *2*, 2681.
[20] J. Wang, S. Yi, J. Liu, S. Sun, Y. Liu, D. Yang, K. Xi, G. Gao, A. Abdelkader, W. Yan, S. Ding, R. V. Kumar, *ACS Nano* **2020**, *14*, 9819.
[21] W. Yao, J. Xu, L. Ma, X. Lu, D. Luo, J. Qian, L. Zhan, I. Manke, C. Yang, P. Adelhelm, R. Chen, *Adv. Mater.* **2023**, *35*, 2212116.
[22] S. Z. Huang, Z. H. Wang, Y. V. Lim, Y. Wang, Y. Li, D. H. Zhang, H. Y. Yang, *Adv. Energy Mater.* **2021**, *11*, 2003689.
[23] X. P. Han, X. F. Ling, Y. Wang, T. Y. Ma, C. Zhong, W. B. Hu, Y. D. Deng, *Angew. Chem., Int. Ed.* **2019**, *58*, 5359.
[24] J. Shen, X. Xu, J. Liu, Z. Liu, F. Li, R. Hu, J. Liu, X. Hou, Y. Feng, Y. Yu, M. Zhu, *ACS Nano* **2019**, *13*, 8986.
[25] Z. Shen, X. Jin, J. Tian, M. Li, Y. Yuan, S. Zhang, S. Fang, X. Fan, W. Xu, H. Lu, J. Lu, H. Zhang, *Nat. Catal.* **2022**, *5*, 555.
[26] Z. Li, C. Zhou, J. Hua, X. Hong, C. Sun, H. W. Li, X. Xu, L. Mai, *Adv. Mater.* **2020**, *32*, 1907444.
[27] W. Hua, H. Li, C. Pei, J. Xia, Y. Sun, C. Zhang, W. Lv, Y. Tao, Y. Jiao, B. Zhang, S. Z. Qiao, Y. Wan, Q. H. Yang, *Adv. Mater.* **2021**, *33*, 2101006.

[28] X. Zhang, Z. Liu, W. Liu, J. Han, W. Lv, *ACS Appl. Mater. Interfaces* **2023**, *15*, 19002.
[29] H. Zhang, Z. Zhao, Y. N. Hou, Y. Tang, J. Liang, X. Liu, Z. Zhang, X. Wang, J. Qiu, *J. Mater. Chem. A* **2019**, *7*, 9230.
[30] J. He, A. Bhargav, A. Manthiram, *ACS Nano* **2021**, *15*, 8583.
[31] Y. Li, X. Wang, M. Sun, J. Xiao, B. Zhang, L. Ai, Z. Zhao, J. Qiu, *ACS Nano* **2022**, *16*, 17008.
[32] Y. Bai, T. T. Nguyen, R. Chu, N. H. Kim, J. H. Lee, *Chem. Eng. J.* **2023**, *454*, 140338.
[33] S. Kim, W.-G. Lim, H. Jung, Y. C. Jeong, C.-Y. Park, S. B. Yang, C. H. Lee, D. Wang, K. Sohn, J. W., Han, J. Lee, *Nat. Commun.* **2025**, *16*, 1649.
[34] X. Ren, Q. Wang, Y. Pu, Q. Sun, W. Sun, L. Lu, *Adv. Mater.* **2023**, *35*, 2304120.
[35] J.-Q. Huang, Q. Zhang, F. Wei, *Energy Storage Mater.* **2015**, *1*, 127.
[36] Y. Xu, W. Yuan, C. Geng, Z. Hu, Q. Li, Y. Zhao, X. Zhang, Z. Zhou, C. Yang, Q.-H. Yang, *Adv. Sci.* **2024**, *11*, 2402497.
[37] L. Ma, Q. Wu, M. He, J. Wu, B. Peng, J. Xu, J. Liu, Z. Jin, *Nano Lett.* **2025**, *25*, 1939.
[38] X. Zhou, R. J. Meng, N. Zhong, S. F. Yin, G. Q. Ma, X. Liang, *Small Methods* **2021**, *5*, 2100571.
[39] F. Ma, Z. Chen, K. Srinivas, D. Liu, Z. Zhang, Y. Wu, M.-q. Zhu, Q. Wu, Y. Chen, *Chem. Eng. J.* **2023**, *459*, 141526.
[40] D. Chinnadurai, R. Rajendiran, O. L. Li, K. Prabakar, *Appl. Catal. B Environ. Energy* **2021**, *292*, 120202.
[41] H.-S. Yang, M.-W. Park, K.-H. Kim, O. L. Li, T.-I. Jeon, J. Kang, *Carbon* **2022**, *189*, 251.
[42] X. Zuo, M. Zhen, D. Liu, L. Fu, Y. Qiu, J. Liu, Y. Zhang, *Adv. Funct. Mater.* **2024**, *34*, 2405486.
[43] L. Xie, Y. Xiao, Q. Zeng, Y. Wang, J. Weng, H. Lu, J. Rong, J. Yang, C. Zheng, Q. Zhang, *ACS Nano* **2024**, *18*, 12820.
[44] M. Yu, D. R. Trinkle, *J. Chem. Phys.* **2011**, *134*, 064111.
[45] J. Liu, G. Li, D. Luo, J. Li, X. Zhang, Q. Li, H. Li, Y. Zhang, Z. Chen, *Adv. Funct. Mater.* **2024**, *34*, 2303357.
[46] L. Zhang, D. Liu, F. Muhammad, W. Wan, Y. Xie, Y. Wang, L. Song, Z. Niu, J. Chen, *Adv. Mater.* **2019**, *31*, 1903955.
[47] X. Zhang, X. Zhou, Y. Wang, Y. Li, *Phys. Chem. Chem. Phys.* **2023**, *25*, 10097.
[48] W. Xiao, K. Yoo, J. H. Kim, H. Xu, *ACS Nano* **2025**, *19*, 23223.
[49] K. Song, J. Liu, H. Dai, Y. Zhao, S. Sun, J. Zhang, C. Qin, P. Yan, F. Guo, C. Wang, Y. Cao, S. Li, W. Chen, *Chem* **2021**, *7*, 2684.
[50] Q. Liang, S. Wang, X. Lu, X. Jia, J. Yang, F. Liang, Q. Xie, C. Yang, J. Qian, H. Song, R. Chen, *ACS Nano* **2024**, *18*, 2395.
[51] C. Zhao, G. L. Xu, Z. Yu, L. C. Zhang, I. Hwang, Y. X. Mo, Y. X. Ren, L. Cheng, C. J. Sun, Y. Ren, X. B. Zuo, J. T. Li, S. G. Sun, K. Amine, T. S. Zhao, *Nat. Nanotechnol.* **2021**, *16*, 166.
[52] F. Y. Fan, W. C. Carter, Y.-M. Chiang, *Adv. Mater.* **2015**, *27*, 5203.
[53] Z. Wang, W. Huang, H. Wu, Y. Wu, K. Shi, J. Li, W. Zhang, Q. Liu, *Adv. Funct. Mater.* **2024**, 2409303.
[54] V. A. de la Peña O'Shea, P. R. de la Piscina, N. Homs, G. Aromí, J. L. G. Fierro, *Chem. Mater.* **2009**, *21*, 5637.
[55] H. Jiang, D. Deng, Y. Kita, M. Hattori, K. Kamata, M. Hara, *J. Am. Chem. Soc.* **2024**, *146*, 20919.
[56] R. Lizárraga, F. Pan, L. Bergqvist, E. Holmström, Z. Gercsi, L. Vitos, *Sci. Rep.* **2017**, *7*, 3778.
[57] X. Zhao, S. Veintemillas-Verdaguer, O. Bomati-Miguel, M. Morales, H. Xu, *Phys. Rev. B* **2005**, *71*, 024106.
[58] M. Wang, X. Zhang, Z. Guo, C. Chen, J. Yuan, Y. Li, Y. Xia, Y.-J. Cheng, *Electrochim. Acta* **2023**, *454*, 142339.
[59] A. Modabberasl, M. Sharifi, F. Shahbazi, P. Kameli, M. Ranjbar, *Diamond Relat. Mater.* **2022**, *128*, 109261.
[60] S. Jeong, S. Kim, H. Son, O. L. Li, *Catal. Today* **2023**, *420*, 114025.
[61] Z. Xie, H. An, X. Zhao, Y. Wang, *Catal. Sci. Technol.* **2022**, *12*, 3148.
[62] Y. J. Li, Z. Z. Wang, H. F. Gu, H. P. Jia, Z. Y. Long, X. Yan, *ACS Nano* **2024**, *18*, 8863.
[63] E. Kim, J. Kim, T. Lee, H. Kang, S. Yu, J. W. Park, S. G. Lee, O. L. Li, J. H. Lee, *Chem. Eng. J.* **2022**, *430*, 132679.
[64] Y. Song, H. Modrow, L. L. Henry, C. K. Saw, E. E. Doomes, V. Palshin, J. Hormes, C. S. S. R. Kumar, *Chem. Mater.* **2006**, *18*, 2817.
[65] L. Meziane, C. Salzemann, C. Aubert, H. Gerard, C. Petit, M. Petit, *Nanoscale* **2016**, *8*, 18640.
[66] S. Chae, S. H. Kim, T. Lee, H. Kang, Y. J. Kwon, G. M. Choi, W. S. Heo, J. B. Park, J.-O. Kim, T. Kwon, B. J. Kim, C. R. Cho, J. W. Park, S. G. Lee, K. Y. Cho, J. H. Lee, *Compos. B* **2023**, *267*, 111050.
[67] O. L. Li, S. Chiba, Y. Wada, G. Panomsuwan, T. Ishizaki, *J. Mater. Chem. A* **2017**, *5*, 2073.
[68] O. L. Li, K. Prabakar, A. Kaneko, H. Park, T. Ishizaki, *Catal. Today* **2019**, *337*, 102.
[69] Y. Li, W. Wang, B. Zhang, L. Fu, M. Wan, G. Li, Z. Cai, S. Tu, X. Duan, Z. W. Seh, J. Jiang, Y. Sun, *Nano Lett.* **2021**, *21*, 6656.
[70] Q. Y. Lu, *ACS Nano* **2024**, *18*, 13973.
[71] Z. Liang, C. Peng, J. Shen, J. Yuan, Y. Yang, D. Xue, M. Zhu, J. Liu, *Small* **2023**, *20*, 2309717.
[72] X. H. Zhao, X. Y. Wu, Q. Q. Hao, Y. S. Liu, K. X. Wang, J. S. Chen, *ACS Appl. Mater. Interfaces* **2024**, *16*, 63647.
[73] Y. Sun, Y. Wang, C. Li, Q. Zhang, L. Wang, Q. Lv, S. Feng, *Adv. Funct. Mater.* **2025**, *35*, 2421780.
[74] K. Akada, S. Obata, K. Saiki, *ACS Omega* **2019**, *4*, 16531.
[75] N. Dimov, A. Staykov, I. M. Kusdhany, S. M. Lyth, *Nanotechnology* **2023**, *34*, 415001.
[76] Y. Song, M. Sun, S. Zhang, X. Zhang, P. Yi, J. Liu, B. Huang, M. Huang, L. Zhang, *Adv. Funct. Mater.* **2023**, *33*, 2214081.
[77] T. Kwon, H. Guo, J.-O. Kim, S. Chae, E. Y. Lim, J. B. Park, E. Lee, I. Choi, B. J. Kim, Y. J. Lee, S. G. Lee, J. H. Lee, *Small* **2024**, *21*, 2407224.
[78] Q. Jiang, H. Xu, K. S. Hui, Z. Ye, C. Zha, Z. Lin, M. Zheng, J. Lu, K. N. Hui, *Angew. Chem., Int. Ed.* **2024**, *136*, 202408474.
[79] B. Li, P. Wang, J. Yuan, N. Song, J. Feng, S. Xiong, B. Xi, *Adv. Mater.* **2024**, *36*, 2309324.
[80] N. Wang, X. Zhang, Z. Ju, X. Yu, Y. Wang, Y. Du, Z. Bai, S. Dou, G. Yu, *Nat. Commun.* **2021**, *12*, 4519.
[81] L. Peng, Z. Wei, C. Wan, J. Li, Z. Chen, D. Zhu, D. Baumann, H. Liu, C. S. Allen, X. Xu, A. I. Kirkland, I. Shakir, Z. Almutairi, S. Tolbert, B. Dunn, Y. Huang, P. Sautet, X. Duan, *Nat. Catal.* **2020**, *3*, 762.
[82] J. Chen, T. Sun, J. Liu, H. Yu, Q. Zang, T. Yuan, F. Zhang, *Adv. Funct. Mater.* **2025**, *35*, 2421780.
[83] J. Wang, W.-Q. Han, *Adv. Funct. Mater.* **2022**, *32*, 2107166.
[84] Z. Liang, J. Shen, X. Xu, F. Li, J. Liu, B. Yuan, Y. Yu, M. Zhu, *Adv. Mater.* **2022**, *34*, 2200102.
[85] J. He, L. Hu, C. Shao, S. Jiang, C. Sun, S. Song, *ACS Nano* **2021**, *15*, 18006.
[86] Z. Q. Ye, Y. Jiang, L. Li, F. Wu, R. J. Chen, *Adv. Mater.* **2021**, *33*, 2101204.
[87] Z. Han, R. Gao, T. Wang, S. Tao, Y. Jia, Z. Lao, M. Zhang, J. Zhou, C. Li, Z. Piao, X. Zhang, G. Zhou, *Nat. Catal.* **2023**, *6*, 1073.
[88] X. Zhao, Y. Zhang, W. Liu, Z. Zheng, Z. Fu, C. Chen, C. Hu, *Adv. Funct. Mater.* **2024**, *34*, 2313107.
[89] S. Hu, X. Huang, L. Zhang, G. Li, S. Chen, J. Zhang, X. Liu, *Adv. Funct. Mater.* **2023**, *33*, 2214161.
[90] S. Hu, T. Wang, B. Lu, D. Wu, H. Wang, X. Liu, J. Zhang, *Adv. Mater.* **2022**, *34*, 2204147.
[91] Q. Shao, L. Xu, D. Guo, Y. Su, J. Chen, *J. Mater. Chem. A* **2020**, *8*, 23772.
[92] M. X. Wang, L. S. Fan, X. Sun, B. Guan, B. Jiang, X. Wu, D. Tian, K. N. Sun, Y. Qiu, X. J. Yin, Y. Zhang, N. Q. Zhang, *ACS Energy Lett.* **2020**, *5*, 3041.
[93] D. Son, J. Kim, W. Zhao, H. Cho, D. G. Lee, J. Son, L. Xu, C.-Y. Park, J. Lee, J. H. Lee, S. Han, H.-T. Kim, T. K. Lee, J. Lee, *ACS Nano* **2025**, *19*, 16611.

[94] J. Pu, S. Fan, Z. Shen, J. Yin, Y. Tan, K. Zhang, B. Wu, G. Hong, Y. F.-F. Yao, *Adv. Funct. Mater.* **2025**, *35*, 2424215.
[95] J. Huangfu, P. Feng, X. Di, Y. Tian, M. Shi, W. Hu, X. Zhao, S. Wang, Y. Xi, F. Kong, H. Wang, *Adv. Energy Mater.* **2025**, *15*, 2502210.
[96] F. Zhou, Z. Gong, R. Wang, M. Guo, R. Zeng, Y. Li, Z. Xiao, L. Qie, J. Liu, *Adv. Funct. Mater.* **2025**, *35*, 2417730.
[97] S. J. Park, Y. J. Choi, H.-S. Kim, M. J. Hong, H. Chang, J. Moon, Y.-J. Kim, J. Mun, K. J. Kim, *Carbon Energy* **2024**, *6*, 487.